


# Ising Machine Based on Electrically Coupled Spin Hall Nano-Oscillators

Brooke C. McGoldrick<sup>1,\*</sup>, Jonathan Z. Sun,<sup>2</sup> and Luqiao Liu<sup>1</sup>

<sup>1</sup>*Department of Electrical Engineering and Computer Science, Massachusetts Institute of Technology, Cambridge, Massachusetts 02139, USA*

<sup>2</sup>*IBM T. J. Watson Research Center, Yorktown Heights, New York 10598, USA*

 (Received 5 August 2021; revised 4 November 2021; accepted 17 December 2021; published 5 January 2022)

The Ising machine is an unconventional computing architecture that can be used to solve NP-hard combinatorial optimization problems more efficiently than traditional von Neumann architectures. Fast, compact oscillator networks that provide programmable connectivities among arbitrary pairs of nodes are highly desirable for the development of practical oscillator-based Ising machines. Here we propose using an electrically coupled array of gigahertz spin Hall nano-oscillators to realize such a network. By developing a general analytical framework that describes injection locking of spin Hall oscillators with large precession angles, we explicitly show the mapping between the coupled oscillators' properties and the Ising model. We integrate our analytical model into a versatile Verilog-A device that can emulate the coupled dynamics of spin Hall oscillators in circuit simulators. With this abstract model, we analyze the performance of the spin Hall oscillator network at the circuit level using conventional electronic components and considering phase noise and scalability. Our results provide design insights and analysis tools toward the realization of a CMOS-integrated spin Hall oscillator Ising machine operating with a high degree of time, space, and energy efficiency.

DOI: [10.1103/PhysRevApplied.17.014006](https://doi.org/10.1103/PhysRevApplied.17.014006)

## I. INTRODUCTION

As Moore's law scaling comes to an end, alternative devices and architectures are becoming necessary to enable further improvements in computing efficiency. One such alternative computing paradigm is the Ising machine, which has been proposed as an efficient combinatorial optimization problem solver. Combinatorial optimization problems are ubiquitous in real-world applications, including artificial intelligence, VLSI circuit design, computer networking, and industries such as steel cutting [1,2]. However, most problems of this class remain unsolvable in their full form due to the inefficiency of von Neumann computing architectures on solving them. On the other hand, the Ising machine hardware naturally solves combinatorial optimization problems by undergoing a dynamic energy minimization process, thereby achieving greater efficiency than existing digital computing schemes.

Ising machines have been realized based on many physical paradigms, including quantum annealing [3], optical parametric oscillators [4], electronic LC [5,6] and phase-transition nano-oscillators [7,8], and most recently spin-based oscillators [9,10]. As opposed to quantum and optical implementations, Ising machines based on electrically coupled oscillators can be operated on chip scale and at room temperature, making this approach most attractive

for scalable computing hardware. Experimental demonstrations of the Ising machine using coupled kilohertz-megahertz electronic oscillators have proven the ability of the oscillator network to solve the Ising model on millisecond time scales [5–8]. However, the Ising machine dynamics can be sped up by orders of magnitude using oscillators operating in the gigahertz frequency range, such as spin torque and spin Hall nano-oscillators (SHNOs). The submicrosecond dynamics of the spin torque oscillator Ising machine was demonstrated in Ref. [10] using a general numerical simulation framework that could be applied to any interoscillator coupling mechanism, such as electrical or magnetic. However, the phenomenological coupling strengths used in the model were not calculated from first principles using physical parameters, making it difficult to determine how the oscillator and system design will impact the coupled network performance. A previous experimental work further showed Ising-like collective dynamics in a small magnetically coupled network of oscillators [9]. While the experimental realization of such a system is a significant milestone, an electrically coupled network will have significant advantages over the magnetic coupling scheme shown therein, as the latter only connects nearest-neighbor oscillators and the coupling strengths are not easily programmable following device fabrication.

In this paper, we present an analytical and numerical study of the electrically coupled SHNO-based Ising machine for the advantages of reaching high

\*bcmgold@mit.edu

connectivities among different nodes as well as tunable connection weights. We first introduce an analytical model that can describe the injection locking dynamics of a SHNO coupled to an external signal at the oscillator's fundamental frequency or harmonics. Different from previous approaches for studying the coupling of SHNOs, we develop an approach—using an impulse sensitivity function derived from the oscillator's magnetization dynamics—to describe the interactions of oscillators not only in small but also large angle oscillation regimes. Based on our analytical model, we develop a Verilog-A macro-model that can emulate the SHNO's injection locking behavior in a standard electrical circuit, which is validated by full micromagnetic simulations. We integrate our oscillator device model into circuit simulations with off-the-shelf electronic components to show how the Ising machine solution time and accuracy are expected to scale with the coupled array size and in the presence of phase noise. Our results provide analytical and quantitative tools to understand the performance of the electrically coupled SHNO network, enabling the future experimental realization of a fast, energy-efficient, and scalable spintronic Ising machine.

## II. OSCILLATOR ISING MACHINE

The mathematical Ising model proposed to describe domain formation in magnetic systems provides the theoretical basis for the Ising machine operation [11]. The Ising Hamiltonian, simplified by neglecting the Zeeman term, is given by [12]

$$H = - \sum_{i,j,i < j}^N J_{ij} s_i s_j, \quad (1)$$

where the  $s_i$  are discrete variables representing spins and the  $J_{ij}$  are exchange coupling coefficients describing the interactions between spins. Under a given  $\{J_{ij}\}$ , spins take values  $s_i = \pm 1$  in order to minimize the system's total energy  $H$ . Many combinatorial optimization problems, including all 21 on Karp's well-known list of NP-hard problems, can be represented by an equivalent Ising Hamiltonian with spins encoding variables to optimize on, and the minimum-energy spin configuration representing the problem's optimal solution [13,14].

A coupled network of nonlinear oscillators as shown in Fig. 1 can be used to solve the Ising model in its collective phase dynamics. When a radio-frequency (rf) signal is applied to a nonlinear oscillator, the oscillator's frequency and/or phase can match that of the external signal by a process known as injection locking. Injection locking is described by the well-known Adler's equation, which can be generalized to describe a coupled network of  $N$

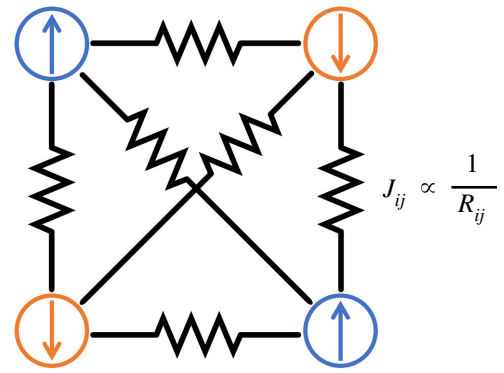


FIG. 1. Schematic of the all-to-all electrically coupled network of four oscillators that can be mapped to the Ising model. Nodes represent oscillators that encode spin values  $s_i = +1$  (“spin up”) or  $s_i = -1$  (“spin down”) in their phases. For resistive coupling, the Ising model coefficients are proportional to the conductances linking each pair of oscillators [5].

oscillators [15,16]

$$\frac{d\psi_i}{dt} = \omega_i - \sum_{j,j \neq i}^N K_{ij} \sin(\psi_i - \psi_j), \quad (2)$$

where  $\psi_i$  and  $\omega_i$  are the phase and frequency of oscillator  $i$  and  $K_{ij}$  is the coupling strength between oscillators  $i$  and  $j$ . By choosing a rotating frame  $\phi_i = \psi_i - \omega^* t$  with respect to the mean oscillator frequency  $\omega^*$ , one further obtains

$$\frac{d\phi_i}{dt} = \omega_i - \omega^* - \sum_{j,j \neq i}^N K_{ij} \sin(\phi_i - \phi_j). \quad (3)$$

For coupled oscillators with close enough frequencies, each oscillator's phase will synchronize to injected signal. This collective process is analogous to the minimization of the oscillator array's equivalent energy  $H$ , called the interaction potential, such that  $d\phi_i/dt = -\partial H/\partial \phi_i$  [16,17]. The interaction potential for an oscillator array described by Eq. (3), neglecting the driving frequency difference, is given explicitly by

$$H = - \sum_{i,j,i \neq j}^N K_{ij} \cos(\phi_i - \phi_j). \quad (4)$$

This takes a similar form to the Ising Hamiltonian in Eq. (1) with coupling coefficients  $K_{ij} = J_{ij}/2$  and oscillator phases representing spins  $\cos(\phi_i - \phi_j) \mapsto s_i s_j = \pm 1$ . However, the oscillator phases are continuous variables whereas the Ising model spins are discrete. To resolve this difference, an effective uniaxial anisotropy is introduced to

the interaction Hamiltonian [16]

$$H = - \sum_{i,j,i \neq j}^N K_{ij} \cos(\phi_i - \phi_j) - K_s \sum_i^N \cos(2\phi_i), \quad (5)$$

where the second term with coupling strength  $K_s$  introduces energy minima at  $\phi_i = \{0, \pi\}$ . The oscillator phases are encouraged to binarize to these values representing discrete spins  $s_i = \pm 1$  in the Ising model. Correspondingly, Adler's equation becomes [5]

$$\frac{d\phi_i}{dt} = \omega_i - \omega^* - \sum_{j,j \neq i}^N K_{ij} \sin(\phi_i - \phi_j) - 2K_s \sin(2\phi_i), \quad (6)$$

where the binarizing term is physically realized by injecting a global second harmonic signal to the coupled oscillator network.

### III. INJECTION LOCKING MODEL

Spin Hall nano-oscillators, or more generally spin torque nano-oscillators, are a type of nonlinear oscillator with a nanometer footprint and gigahertz oscillation frequency originating from the direct-current-induced spontaneous magnetic precession [Figs. 2(a) and 2(b)] [18,19]. Generally, one relies on numerical solutions to describe

the oscillation dynamics of the magnetic moments as well as their interactions with external signals. Previously, in the seminal works [20,21], Slavin *et al.* derived a compact analytical model describing injection locking of spin torque oscillators. Initially, this model only treated small angle precession in the near-threshold regime before being extended in Ref. [22] to large angle circular precession trajectories. However, it still remains a challenging task to model injection locking in oscillators with nontrivial precession trajectories such as the ‘‘clamshell’’ orbit. Moreover, the lack of freedom on the trajectory shape makes it challenging to account for injection locking at higher harmonic frequencies, which relies on the deviation of the magnetic moment precession from a perfect circular or elliptical shape.

Here, in order to characterize the injection locking behavior for practical SHNOs with large oscillation angles, we employ an alternative approach using the impulse sensitivity function (ISF) of the SHNO. The ISF is a characteristic function of a nonlinear oscillator describing the time-varying phase and amplitude sensitivity to perturbation by an external signal [23]. With the ISF, we derive an analytical expression for the injection locking strength of the SHNO based on the oscillation orbit, which can be used directly as an input parameter in Adler's equation. Our model comprehensively describes the injection locking behavior of a SHNO with any orbital trajectory and at both the fundamental and harmonic frequencies.

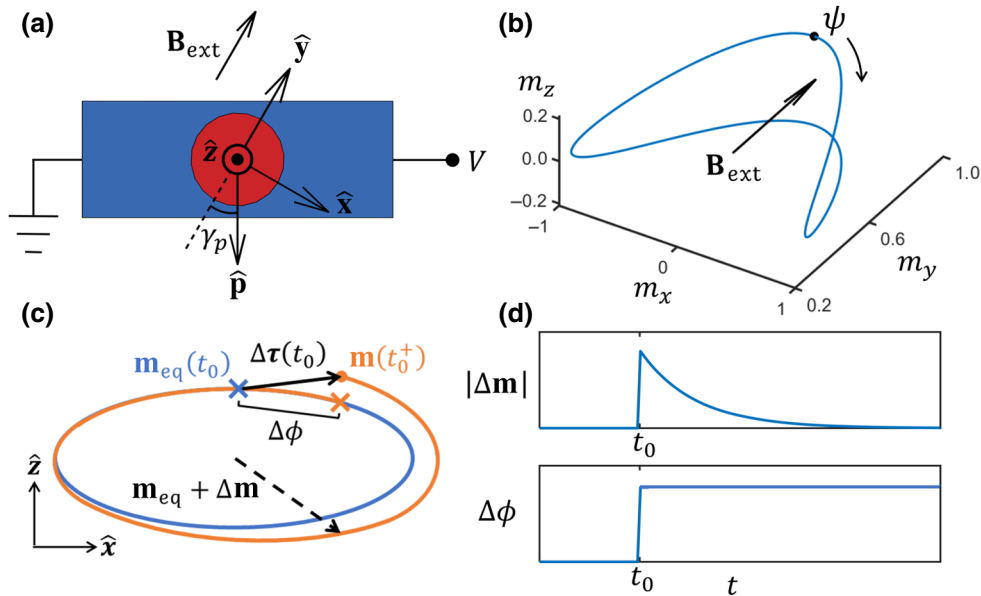


FIG. 2. (a) Top view of a three-terminal SHNO. Blue is heavy metal and red is the magnetic tunnel junction (MTJ) stack (from top to bottom, consisting of a static magnetic fixed layer, insulating spacer layer, and precessing magnetic free layer adjacent to heavy metal). (b) Clamshell-shaped equilibrium precession  $\mathbf{m}_{eq}$  of the in-plane magnetized SHNO calculated in a micromagnetic simulation using the parameters in Appendix A. (c) Schematic of the SHNO's magnetization precession orbit subject to an impulse perturbation at time  $t_0$  (blue cross). Blue (orange) orbits represent equilibrium (perturbed) precession. The orange cross shows the phase deviation of the oscillator one period after perturbation. (d) Amplitude and phase response of the perturbed oscillator in (c).

Despite being a nonlinear oscillator, the phase response of the SHNO to external perturbations at a given operating point can be described by an impulse response function. For a general nonlinear oscillator, the phase response to an impulse perturbation applied at time  $t_0$  is [23–25]

$$h_\phi(t, t_0) = \omega_g \Gamma(t_0) u(t - t_0), \quad (7)$$

where  $\omega_g$  is the unperturbed oscillator frequency,  $u(t - t_0)$  is a unit step, and the coefficient  $\Gamma(t_0)$  is the ISF that reflects the oscillator's phase sensitivity to external perturbations over each period. This phase impulse response for the SHNO is illustrated in Figs. 2(c) and 2(d). Under this linear treatment of the phase response, the ISF includes all the information about the oscillator's nonlinearity through its dependence on the equilibrium oscillation orbit. The net phase change under an arbitrary perturbing signal  $P(t)$  can be written as [23]

$$\Delta\phi(t) = \int_{-\infty}^{\infty} h_\phi(t, \tau) P(\tau) d\tau = \omega_g \int_{-\infty}^t \Gamma(\tau) P(\tau) d\tau. \quad (8)$$

Meanwhile, orbital deviations are amplitude limited and decay once the perturbation is removed due to the restoring force of the nonlinear oscillator to its equilibrium trajectory [Figs. 2(c) and 2(d)], and are therefore neglected [23–25]. For the nonlinear SHNO, we can verify that this linear phase assumption remains valid as long as the perturbing signal is not much larger than the dc biasing force (see the discussion in Sec. III B).

Previously, the ISFs of other oscillators have been calculated using various approaches such as nonlinear perturbation theory [24,26], direct measurement of the oscillator's phase response to impulse perturbations [25,27,28], or analytically calculating the phase shifts by projecting the perturbation along the equilibrium oscillation trajectory [23]. We use the third method because it allows us to construct an intuitive expression for the ISF based on the SHNO's magnetization dynamics.

As a first step in deriving the ISF, we describe the equilibrium precession of the in-plane magnetized SHNO. The Landau-Lifshitz-Gilbert-Slonczewski (LLGS) equation is used to describe the magnetization precession dynamics [29–31]

$$\frac{d\mathbf{m}}{dt} = -\frac{\gamma_e}{1 + \alpha^2} \{\mathbf{m} \times \mathbf{B}_{\text{eff}} + \alpha[\mathbf{m} \times (\mathbf{m} \times \mathbf{B}_{\text{eff}})] + B_s[\mathbf{m} \times (\mathbf{m} \times \hat{\mathbf{p}})] - \alpha B_s(\mathbf{m} \times \hat{\mathbf{p}})\}, \quad (9)$$

where  $\gamma_e$  is the electron gyromagnetic ratio,  $\alpha$  is the Gilbert damping parameter,  $\mathbf{m}$  is the normalized free layer magnetization,  $\mathbf{B}_{\text{eff}}$  is the effective magnetic field,  $B_s$  is the spin torque field, and  $\hat{\mathbf{p}}$  is the injected spin polarization direction. The spin torque term proportional to  $\alpha B_s$  has the same

symmetry as the fieldlike torque and is usually neglected. Under stable oscillation, the torque from the dc current counterbalances the magnetic damping and maintains the equilibrium oscillation orbit. Therefore, we can separate the torques on the right-hand side of Eq. (9) into two parts,

$$\begin{aligned} \frac{d\mathbf{m}}{dt} &= -\gamma_e \{\mathbf{m} \times \mathbf{B}_{\text{eff}} + \alpha[\mathbf{m} \times (\mathbf{m} \times \mathbf{B}_{\text{eff}})] \\ &\quad + (B_{s0} + b_{\text{srf}})[\mathbf{m} \times (\mathbf{m} \times \hat{\mathbf{p}})]\} \\ &= \boldsymbol{\tau}_{\text{eq}} + \boldsymbol{\tau}_{\text{rf}}, \end{aligned} \quad (10)$$

where the dc and rf components of  $B_s$  are separated based on the voltages applied to the heavy metal in Fig. 2(a):

$$(B_{s0} + b_{\text{srf}})\hat{\mathbf{p}} = \frac{\sigma}{R_{\text{HM}}} (V_{\text{dc}} + V_{\text{rf}}) \begin{pmatrix} \sin(\gamma_p) \\ -\cos(\gamma_p) \\ 0 \end{pmatrix}. \quad (11)$$

Here  $R_{\text{HM}}$  is the total resistance of the heavy metal strip,  $\gamma_p$  is the spin polarization angle shown in Fig. 2(a), and  $\sigma = \hbar\theta_{\text{SH}}/(2eM_s A t_{\text{FL}})$ , where  $\theta_{\text{SH}}$  is the spin Hall angle,  $M_s$  is the free layer saturation magnetization,  $A$  is the cross-sectional area of the heavy metal, and  $t_{\text{FL}}$  is the free layer thickness. A voltage bias applied across the MTJ for readout will introduce an additional dc spin transfer torque term in Eq. (10); however, this is estimated to be an order of magnitude smaller than the spin orbit torque excitation due to  $V_{\text{dc}}$ , and is therefore neglected.

In describing the equilibrium precession, we assume that the rf spin torque field  $b_{\text{srf}}$  is relatively weak compared to the dc component  $B_{s0}$ . One can then numerically solve the LLGS equation considering only  $\boldsymbol{\tau}_{\text{eq}}$  in macrospin or micromagnetic simulations to find the equilibrium precession (see Appendix A for our simulation details). A typical equilibrium orbit is shown in Fig. 2(b). Considering the lowest (dominant) harmonic for each spatial component, this can be approximated by

$$\mathbf{m}_{\text{eq}} = \begin{pmatrix} m_x \sin(\psi) \\ m_{y0} + m_y \cos(2\psi) \\ m_z \cos(\psi) \end{pmatrix} \quad (12)$$

with the total oscillator phase  $\psi = \omega_g t + \phi$ . For the considered case, the magnetic moment only develops a very small equilibrium component along the  $x$  axis under the spin torque and effective magnetic fields, so we choose  $m_{x0} \approx 0$  and verify that its existence does not lead to any significant deviation from the results shown below. Notably, due to the clamshell-shaped precession, the magnetization  $y$  component oscillates at twice the frequency of the  $x$  and  $z$  components. In the following sections, we will see that this enables strong injection locking at the second harmonic. This second harmonic injection locking is analogous to parametric pumping of spin waves by a rf magnetic field applied parallel to the static magnetization direction at twice the magnon frequency [32–35].

### A. Impulse sensitivity function

We derive the ISF by analytically projecting the spin torque perturbation along the equilibrium precession trajectory to calculate the resulting phase shifts. This technique was originally proposed by Hajimiri *et al.* for general nonlinear oscillators [23]. Here, we extend this method to the SHNO based on the magnetization dynamics described by the LLGS equation. Our general expression is used to predict the injection locking sensitivity to an applied time-varying voltage.

First, consider a SHNO with equilibrium magnetization precession given by  $\mathbf{m}_{\text{eq}}(t)$  in Eq. (12). Considering a perturbing impulse torque  $\Delta\boldsymbol{\tau}(t)\delta(t-t_0)$ , we expect a response of the oscillator magnetization  $\mathbf{m}(t_0^+) = \mathbf{m}_{\text{eq}}(t_0) + \Delta\boldsymbol{\tau}(t_0)$  [Fig. 2(c)]. Because we neglect amplitude deviations, we only consider the component of  $\Delta\boldsymbol{\tau}$  along the equilibrium precession trajectory. The displacement  $l$  along the precession trajectory is then given by  $\Delta\boldsymbol{\tau}$  dotted with a unit vector along the trajectory direction:

$$l = \Delta\boldsymbol{\tau}(t) \cdot \frac{\dot{\mathbf{m}}_{\text{eq}}(t)}{|\dot{\mathbf{m}}_{\text{eq}}(t)|}. \quad (13)$$

We then divide by the instantaneous precession speed  $|\dot{\mathbf{m}}_{\text{eq}}|$  to find the equivalent phase shift in units of time:

$$\Delta\phi_l = \Delta\boldsymbol{\tau}(t) \cdot \frac{\dot{\mathbf{m}}_{\text{eq}}(t)}{|\dot{\mathbf{m}}_{\text{eq}}(t)|^2}. \quad (14)$$

Normalizing the phase shift with the magnitude of the perturbation, we obtain the ISF for a SHNO perturbed by a voltage  $V$ :

$$\Gamma_s(t) = \frac{\Delta\boldsymbol{\tau}(t)}{V} \cdot \frac{\dot{\mathbf{m}}_{\text{eq}}(t)}{|\dot{\mathbf{m}}_{\text{eq}}(t)|^2}. \quad (15)$$

For the stable solution in Eq. (12), one can calculate the ISF with Eq. (15) and express it in the form of a Fourier series, i.e.,

$$\begin{aligned} \Gamma_s(t) = \frac{\omega_g \gamma_e \sigma}{4R_{\text{HM}} |\dot{\mathbf{m}}_{\text{eq}}|^2} & \left[ \sum_{n=\text{odd}} p_x a_n \frac{1}{n^2} \cos[n(\omega_g t + \phi)] \right. \\ & \left. + \sum_{n=\text{even}} p_y b_n \frac{1}{n^2} \sin[n(\omega_g t + \phi)] \right] \end{aligned} \quad (16)$$

with nonzero coefficients

$$\begin{aligned} a_1 &= 2m_x[m_y^2 + 4m_y m_{y0} + 2(m_{y0}^2 + m_z^2)], \\ a_3 &= 3m_x m_y^2, \\ a_5 &= -m_x m_y^2, \\ b_2 &= -2[m_x^2(2m_y + m_{y0}) + m_z^2(2m_y - m_{y0})], \\ b_4 &= m_y(m_x^2 - m_z^2), \end{aligned}$$

where the instantaneous precession speed is

$$\begin{aligned} |\dot{\mathbf{m}}_{\text{eq}}|^2 &= \frac{\omega_g^2}{2} \{ (m_x^2 + 4m_y^2 + m_z^2) \\ &+ (m_x^2 - m_z^2) \cos[2(\omega_g t + \phi)] \\ &- 4m_y^2 \cos[4(\omega_g t + \phi)] \}. \end{aligned} \quad (17)$$

Figure 3(a) shows the ISF calculated for a SHNO with a typical clamshell oscillation orbit. Here, we have plotted separately the odd- and even-harmonic series of Eq. (16) proportional to spin polarization components that are asymmetric ( $p_x$ ) and symmetric ( $p_y$ ) with respect to the precession trajectory [36].

### B. Adler's equation

The ISF contains all necessary information for describing injection locking of the SHNO, allowing us to relate Adler's equation coefficients [Eq. (6)] with the oscillator's physical properties. We define  $\phi(t)$  as the phase in the rotating frame as in Eq. (3), and from Eq. (8), we have

$$\phi(t) = (\omega_g - \omega_e)t + \omega_g \int_{-\infty}^t \Gamma_s(\tau) P(\tau) d\tau, \quad (18)$$

where  $\omega_e$  is the external signal frequency. Calculating the derivative with respect to  $t$  on both sides of Eq. (18), we obtain [28]

$$\frac{d\phi(t)}{dt} = \omega_g - \omega_e + \omega_g \Gamma_s(t) P(t). \quad (19)$$

Because the phase evolution  $d\phi/dt$  that contributes to the long-term dynamics is much slower than the oscillatory dynamics, we can approximate the right-hand side by the average over one period [16]:

$$\frac{d\phi(t)}{dt} = \omega_g - \omega_e + \frac{\omega_g}{T} \int_t^{t+T} \Gamma_s(t') P(t') dt'. \quad (20)$$

Consider an injection locking signal that contains both first and second harmonic components:

$$P(t) = V_{1f} \sin[\omega_e t + \phi_{e1}] + V_{2f} \cos[2(\omega_e t + \phi_{e2})]. \quad (21)$$

Substituting Eqs. (16) and (21) into Eq. (20), we see that the only relevant terms of  $\Gamma_s$  that contribute to the long-term phase variations are

$$\begin{aligned} \Gamma_s(t) &= \frac{\gamma_e \sigma p_x}{2\omega_g R_{\text{HM}}} a'_1 \cos(\omega_e t + \phi) \\ &+ \frac{\gamma_e \sigma p_y}{4\omega_g R_{\text{HM}}} b'_2 \sin[2(\omega_e t + \phi)] \\ &= \Gamma_{1f}(t) + \Gamma_{2f}(t), \end{aligned} \quad (22)$$

where  $a'_1$  and  $b'_2$  are calculated by approximating Eqs. (16) and (17) to second order and finding the Fourier series

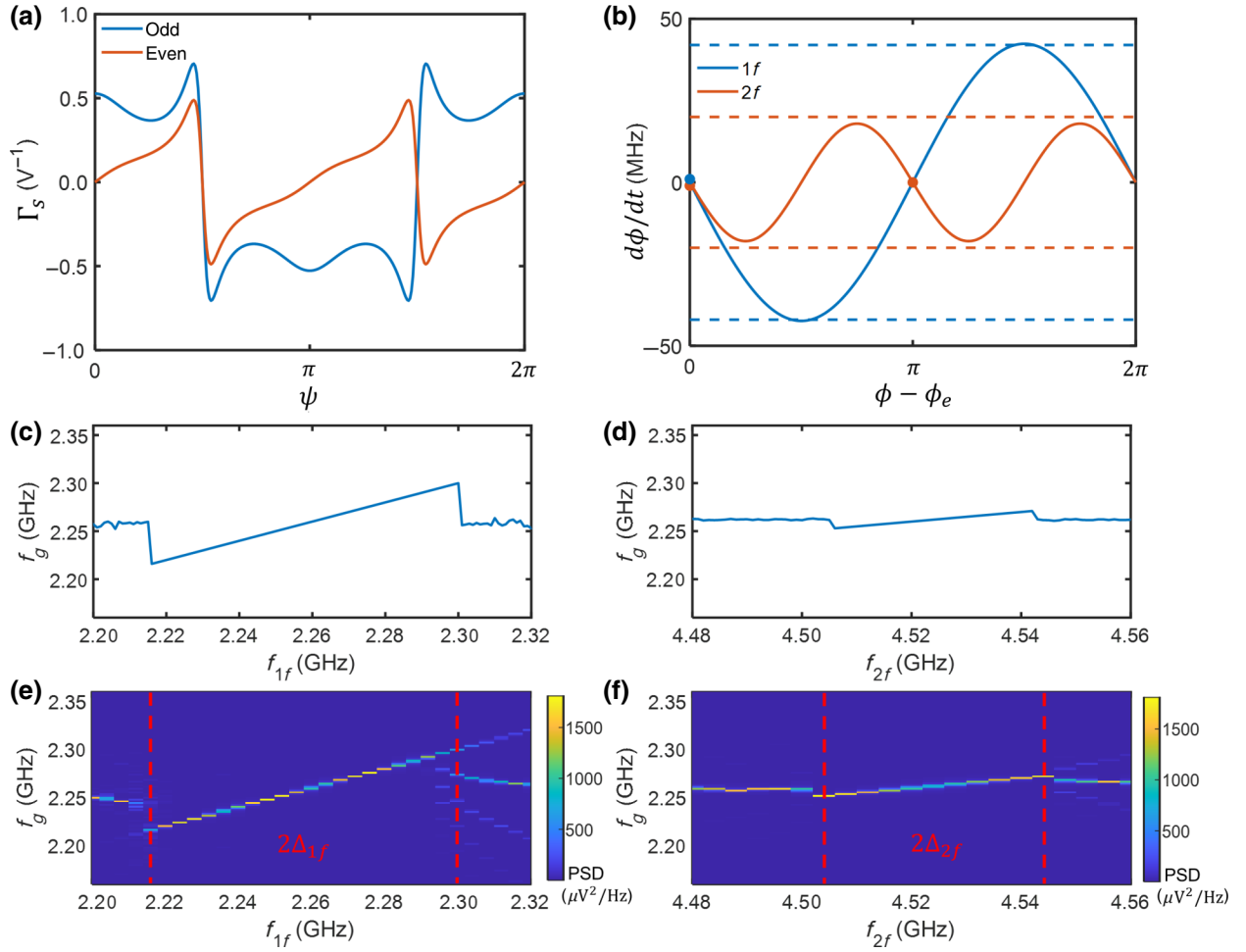


FIG. 3. ISF and Adler's equation for a device with the parameters given in Appendix A. (a) Odd and even series of the SHNO ISF [Eq. (16)] based on a typical clamshell orbit. (b) Solid lines show Adler's equation [Eq. (23)] predictions with  $V_{1f} = -V_{2f} = 66$  mV. The  $2f$  component's amplitude is doubled to account for the second harmonic frequency. Dotted lines are phase locking bandwidths  $\Delta = |d\phi/dt|$  calculated in micromagnetic simulations (e),(f). The injection locking strength predicted by Eq. (23) very closely matches the simulated phase locking bandwidth, showing that our ISF model can accurately predict injection locking at the first and second harmonics. We can also tell the stable phase locking angles (marked by dots) between the oscillator and external signal where  $d\phi/dt = 0$  and  $d^2\phi/dt^2 < 0$ . At the first harmonic, the oscillator is expected to lock-in phase with the external signal, while the second harmonic signal gives bistable locking that binarizes the phases as described in Sec. II. (c),(d) Phase locking bandwidths calculated by numerically integrating Eq. (23) with  $V_{rf} = 66$  mV at (c) the first harmonic  $f_{1f} \approx f_g$  and (d) the second harmonic  $f_{2f} \approx 2f_g$ . (e),(f) Power spectral density of SHNO calculated in micromagnetic simulations under injection locking at (e) the first harmonic and (f) the second harmonic. The phase locking bandwidths are marked by vertical dotted lines, showing the boundaries of the region where the oscillator phase locks to the external signal.

coefficients

$$a'_1 = \frac{x_1}{y} \left( 1 - \sqrt{\frac{|y-1|}{|y+1|}} \right),$$

$$b'_2 = \frac{x_2}{y^2} (1 - \sqrt{|y^2-1|}),$$

$$x_1 = \frac{a_1}{m_x^2 + 4m_y^2 + m_z^2},$$

$$x_2 = \frac{b_2}{m_x^2 + 4m_y^2 + m_z^2},$$

$$y = \frac{m_x^2 - m_z^2}{m_x^2 + 4m_y^2 + m_z^2}.$$

Note that the higher order terms of  $\Gamma_s$  in Eq. (16) lead to fast phase oscillations that do not accumulate beyond one period and are therefore neglected. Finally, evaluating Eq. (20) gives us Adler's equation for the SHNO:

$$\begin{aligned} \frac{d\phi(t)}{dt} = & \omega_g - \omega_e - \frac{\gamma_e \sigma P_x}{4R_{HM}} a'_1 V_{1f} \sin(\phi - \phi_{e1}) \\ & + \frac{\gamma_e \sigma P_y}{4R_{HM}} b'_2 V_{2f} \sin[2(\phi - \phi_{e2})]. \end{aligned} \quad (23)$$

Comparing to Eq. (6), we have extracted the coupling coefficients of Adler's equation in terms of the material and device parameters that possess real physical meanings. The first and second harmonic terms of Eq. (23) are plotted separately in Fig. 3(b). While this equation describes the injection locking of a single oscillator, it can be trivially extended to a coupled network of oscillators as in Eq. (6) (see Sec. IV B).

To demonstrate that our model can accurately predict first and second harmonic injection locking, we numerically evaluate Eq. (23) to find the injection locked oscillator's frequency as a function of  $f_e = \omega_e/2\pi$ . We apply a rf perturbing signal  $P(t) = V_{\text{rf}} \sin(\omega_e t)$  to the free-running oscillator and sweep the frequency  $\omega_e$  about  $\omega_g$  and  $2\omega_g$  for first and second harmonic injection locking, respectively. We obtain the results in Figs. 3(c) and 3(d). We then carry out micromagnetic simulations with the same device parameters and rf voltages. In Figs. 3(e) and 3(f), we show the power spectral density of the oscillator's microwave output voltage as a function of  $f_e$ , from which one sees that Eq. (23) and the full micromagnetic simulations lead to the same calculated coupling bandwidths.

Furthermore, we evaluate the coupling bandwidths as a function of the injection locking signal amplitude in Fig. 4, comparing our analytical model and micromagnetic simulations. For coupling signal amplitudes up to  $V_{\text{rf}} \approx V_{\text{dc}}$ , the bandwidths calculated in micromagnetic simulations follow the linear trend predicted by Eq. (23), demonstrating that our ISF-based model holds across a wide range of coupling signals. For coupling signal amplitudes above this threshold, this linear assumption will begin to break down due to large modulation of the oscillation amplitude by the rf signal. This gives rise to further effects, such as matching between the oscillator's nonlinear eigenfrequency and the external signal frequency via coupling between the oscillator's amplitude and phase, that are not represented in this model [21].

#### IV. CIRCUIT-LEVEL SIMULATION

To reliably predict the performance of the SHNO Ising machine, we need to simulate large arrays up to hundreds or thousands of coupled oscillators. To do so, we develop a computationally lightweight SHNO macromodel based on our analytical ISF. The oscillator macromodel is integrated with off-the-shelf electronic components in circuit simulations to realize a tunable electrical coupling scheme. We show that our macromodel can accurately replicate the collective phase dynamics of a SHNO array calculated in micromagnetic simulations but in a very small percentage of the computation time.

##### A. Verilog-A oscillator macromodel

We introduce an ISF-based macromodel of the SHNO in Verilog-A that emulates the oscillator's electrical behavior,

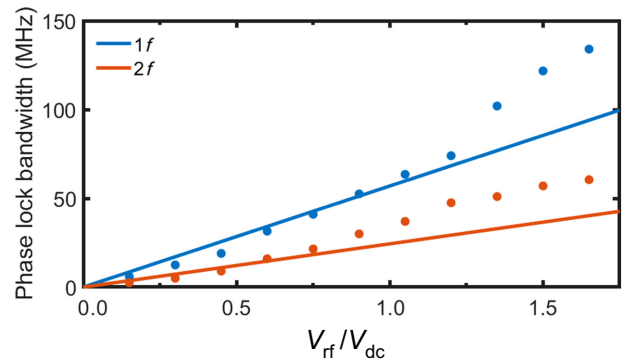


FIG. 4. Phase locking bandwidth as a function of the injection locking signal strength at first and second harmonics. Lines represent bandwidths calculated from ISF [coefficients of Eq. (23)], while scatters are the corresponding bandwidths obtained from micromagnetic simulations based on the device parameters in Appendix A.

nonlinear phase dynamics, and thermal phase noise characteristic [37–41]. Verilog-A is an analog circuit modeling language that enables the development of custom device models for circuit-level simulations, including SHNOs [42–45]. Detailed  $I$ - $V$  relations are defined within the Verilog-A device model to describe its behavior, with an abstract interface of input and output ports for integration with other components in circuit-level simulations [46]. Previous approaches to model the spin torque oscillator at the circuit level have involved numerically simulating the LLGS equation using an equivalent circuit representation [47–49], which is computationally expensive, or solving analytical equations that accurately model the electrical behavior, including output power and linewidth, but do not include nonlinear injection locking [42–45,50]. On the other hand, our analytical ISF-based approach comprehensively models the nonlinear behavior of the oscillator without requiring heavy computation. The macromodel code described below is open source and available online [51].

A functional block diagram of the SHNO macromodel is shown in Fig. 5(a). The user-input material and device parameters are specified in Table I with values given for the SHNO studied here. The oscillator's free-running angular frequency  $\omega_g$  and components of  $\mathbf{m}_{\text{eq}}$  [to leading order, as in Eq. (12)] in the top block of Fig. 5(a) can be input as a function of  $V_{\text{dc}}$  to model the oscillator across a range of operating points. These values can be extracted from a one-time micromagnetic or macrospin simulation of the SHNO device and imported to Verilog-A as look-up tables.

In the initial circuit simulation timestep, the oscillator macromodel undergoes a dc operating point analysis. First,  $V_{\text{dc}}$  is sampled to determine  $\omega_g$  and  $\mathbf{m}_{\text{eq}}$  at the given operating point. Then, the ISF is calculated from Eq. (16). While we have only provided the ISF for in-plane

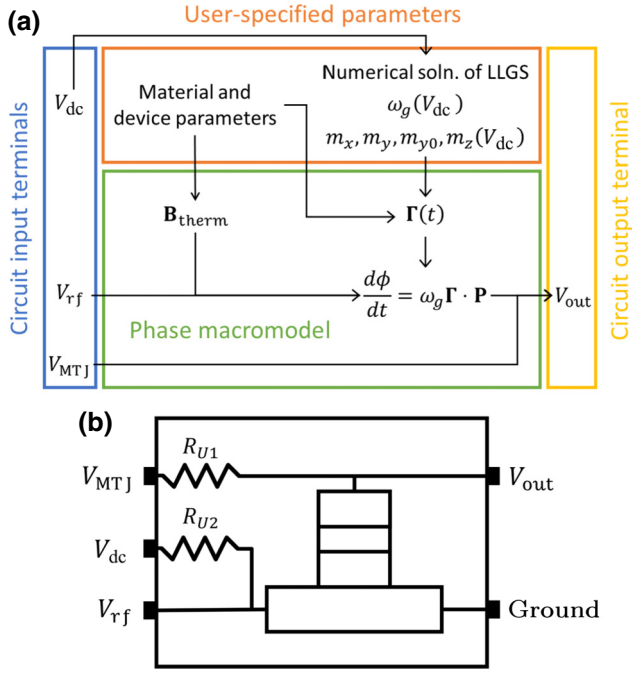


FIG. 5. (a) Block diagram of the SHNO macromodel implemented in Verilog-A, including electrical behavior and the non-linear phase macromodel to calculate injection locking and phase noise. (b) Circuit-level symbol of SHNO showing electrical terminals and pull-up resistors  $R_{U1}, R_{U2}$ .

precession, a similar derivation as in Sec. III A can be carried out for any arbitrary precession orbit and coded into Verilog-A.

Besides injection locking by deterministic electrical signals, the ISF approach can be used to model phase noise due to stochastic thermal fluctuations [41]. Thermal fluctuations can be treated as an effective field in the macrospin approximation [52,53]

$$\mathbf{B}_{\text{therm}} = \eta(t) \sqrt{\frac{2\alpha k_B T}{\gamma_e V_{\text{FL}} M_s \Delta t}}, \quad (24)$$

where  $\eta(t)$  is a three-dimensional Cartesian vector with components randomly chosen from a normal distribution every  $\Delta t$ ,  $T$  is the temperature, and  $V_{\text{FL}}$  is the volume of the oscillator's free layer. Because the ISF is a characteristic of the oscillator and independent of the perturbation waveform, the effective thermal field ISF is derived by a similar process as for the spin torque ISF. The ISFs corresponding to perturbation by effective magnetic fields along  $x$ ,  $y$ , and  $z$  directions are calculated in Appendix B and integrated into the oscillator macromodel in analytical form.

As we showed in Sec. III B, the dynamic phase behavior of the SHNO is well captured by Adler's equation with our analytically derived coupling coefficients. Because Adler's equation is a simple first-order differential equation, it can be solved very efficiently in the form shown in Fig. 5(a)

TABLE I. User-specified material and device parameters in the Verilog-A SHNO macromodel, including frequency and equilibrium precession components at the given operating point  $V_{\text{dc}}$ . The values given are those used in our simulations.

Parameter	Symbol	Value	Unit
Parallel MTJ resistance	$R_P$	1200	$\Omega$
Antiparallel MTJ resistance	$R_{AP}$	2400	$\Omega$
Heavy metal resistance	$R_{HM}$	200	$\Omega$
Heavy metal width	$w_{HM}$	200	nm
Heavy metal thickness	$t_{HM}$	5	nm
Spin polarization angle	$\gamma_p$	30	deg
Spin Hall angle	$\theta_{SH}$	0.07	
Gilbert damping	$\alpha$	0.02	
Saturation magnetization	$M_s$	800	kA/m
MTJ width	$w_{MTJ}$	120	nm
MTJ length	$l_{MTJ}$	200	nm
Free layer thickness	$t_{FL}$	1.5	nm
Thermal field timestep	$\Delta t$	15	ps
MTJ voltage	$V_{MTJ}$	300	mV
MTJ pull-up resistor	$R_{U1}$	500	$\Omega$
dc voltage	$V_{dc}$	176	mV
Heavy metal pull-up resistor	$R_{U2}$	200	$\Omega$
Free-running frequency	$\omega_g(V_{dc})$	2.26	GHz
Components of $\mathbf{m}_{\text{eq}}(V_{dc})$	$m_x$	0.99	
	$m_y$	0.34	
	$m_{y0}$	0.6	
	$m_z$	0.21	

using general SPICE-based analog circuit simulators. The phase responses to spin torque and thermal field perturbations are calculated in parallel by multiplying each ISF with the corresponding perturbation and summing the total contribution to the phase at each timestep.

Finally, we package the analysis above into a compact SHNO device model as shown in Fig. 5(b). The device interacts with the external circuit only through its input terminals including MTJ bias voltage  $V_{\text{MTJ}}$ , dc driving voltage  $V_{\text{dc}}$ , and rf locking signal  $V_{\text{rf}}$ , as well as its output terminal  $V_{\text{out}}$ . The effective resistance across each pair of electrical terminals is modeled based on the heavy metal and MTJ resistances, including the rf oscillating magnetoresistance of the nanopillar. These resistances are used to construct the MTJ's electrical output signal

$$V_{\text{out}} = \frac{V_{\text{MTJ}}}{R_{\text{MTJ}} + R_{U1}} \times \left( R_{\text{MTJ}} + \frac{R_P - R_{AP}}{2} m_x \sin[\omega_g t + \phi(t)] \right), \quad (25)$$

where  $R_{\text{MTJ}} = (R_{AP} + R_P + R_{HM})/2$  is the equivalent dc resistance between the MTJ readout terminal and ground. Here we assume that the fixed layer of the MTJ is oriented along the  $+x$  axis due to shape anisotropy.



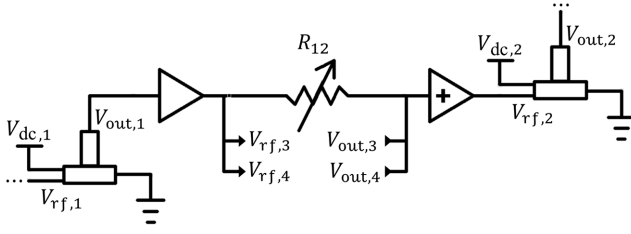


FIG. 6. HSPICE coupling circuit schematic using the SHNO macromodel and off-the-shelf amplifier models. One full coupling branch is shown for the all-to-all connected network in Fig. 1 with oscillators arbitrarily numbered 1–4. Auxiliary gain-setting resistors and dc biasing elements are omitted for visual clarity.

### B. Coupled oscillator array

Using our Verilog-A SHNO device model, we can directly construct a coupled oscillator network and simulate its performance at the circuit level. We use HSPICE, a commercial variant of the SPICE-based analog circuit simulators with notably high performance and accuracy, which is employed in related works on SHNO-based computing schemes [54,55]. One branch of the electrical coupling circuit simulated in HSPICE is shown in Fig. 6. A buffer on the oscillator output is used to match the SHNO impedance with the following stage and a rf gain block ensures an adequate coupling signal amplitude. We use simulation models of Texas Instruments LMH5401 and Texas Instruments TRF37D73 for these two devices. The buffer has a fully differential architecture that provides oscillator outputs of both positive and negative polarities to the coupling circuit, allowing problems with any coupling coefficient signs to be modeled. The coupling conductances are set by variable resistors such as voltage-programmable memristors [56]. The first harmonic coupling signal to the input of node  $i$  is given by

$$V_{1f} \sin(\omega_g t + \phi_{e1}) = A_v \sum_{j=1}^N |V_{\text{out},j}| \frac{R_{\text{HM}}}{R_{ij}} \sin(\omega_g t + \phi_j), \quad (26)$$

where  $A_v = 5.5$  is the net signal loop gain,  $|V_{\text{out},j}|$  is the amplitude of the output signal from oscillator  $j$  in Eq. (25) (with dc component filtered), and  $R_{ij}$  is the resistance linking oscillators  $i$  and  $j$ . Substituting into Eq. (23), we note that the Ising model coefficients in this coupling scheme will be proportional to the tunable internode conductances  $1/R_{ij}$ . Finally, in a realistic circuit, delay lines need to be designed such that any finite parasitic phase shift around the coupling loop is compensated, avoiding associated time-delay coupling complications [28,57–59]. The impact of such time delay on the coupling dynamics is briefly discussed in Appendix D.

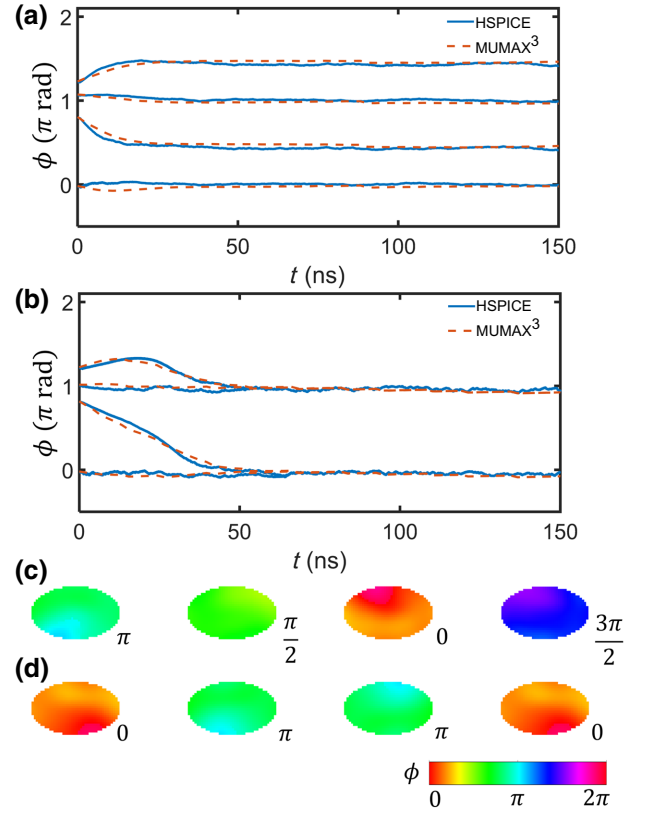


FIG. 7. Phase dynamics of the four-node all-to-all coupled network solving the Ising model with  $J_{ij} = -1$  in HSPICE and MUMAX<sup>3</sup> (neglecting thermal noise) (a) with first harmonic coupling only and (b) with the addition of a binarizing second harmonic signal. Without second harmonic locking (a), the phases spread across  $0-2\pi$  and the ground state is not clearly visible. Once a second harmonic signal is applied (b), the phases clearly binarize and settle to the ground state  $\{\phi\} = \{0, 0, \pi, \pi\}$ . (c),(d) Spatial plots of the free layer magnetization phase in MUMAX<sup>3</sup> corresponding to the final phase configuration at  $t = 150$  ns in (a) and (b), respectively. Interscillator spacing has been reduced for visibility.

To obtain a baseline result for the coupling behavior, we simulate four all-to-all coupled oscillators (Fig. 1) in HSPICE with uniform coupling  $J_{ij} = -1$  where the minimum-energy (ground-state) phase configuration corresponds to any permutation of  $\{\phi\} = \{0, 0, \pi, \pi\}$ . Meanwhile, to verify the validity of the circuit simulations, we replicate the same problem in micromagnetic simulations by modifying the open-source MUMAX<sup>3</sup> code to support electrical signal generation and coupling as described in Appendix C. The simulated phase dynamics from these two parallel approaches are shown in Figs. 7(a) and 7(b). In Fig. 7(a), only the first harmonic injection locking signal is introduced to each node, while in Fig. 7(b), a global second harmonic signal is included with amplitude  $V_{2f} = 40$  mV. With the second harmonic signal, the phases of the SHNOs binarize and arrive at the ground-state solution.

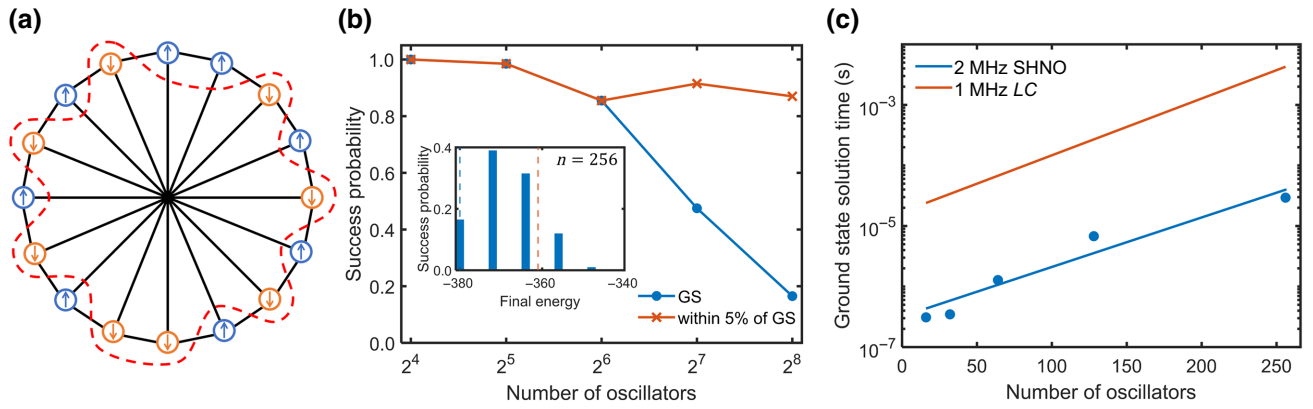


FIG. 8. (a) Sixteen-node Mobius ladder graph architecture used in Sec. V. The MAX-CUT solution for an unweighted graph ( $w_{ij} = 1$ ) is shown by the dotted line partitioning the graph into two opposite-spin subgraphs. (b) Probability of reaching the ground state (GS) and within 5% of the GS versus  $n$ . Inset: histogram of final energy states for  $n = 256$  (blue dotted line is  $E_{GS} = -380$ , orange dotted line is within 5% of the GS). (c) Solution time of the SHNO Ising machine (blue scatters) as a function of  $n$ . The blue line shows the trend. The orange line represents the expected solution time of a 1 MHz LC oscillator Ising machine, reproduced from Chou *et al.* [6] (licensed under CC BY 4.0 [60]).

Spatial plots of the magnetization phase of the unbinarized and binarized oscillators from micromagnetic simulations are also shown in Figs. 7(c) and 7(d). The key features of the phase dynamics, including time-to-solution and the steady-state configuration, are very well matched between micromagnetic and circuit simulations. Slight discrepancies in the shape of the phase curves can be attributed to the more abstract macrospin-based modeling used in HSPICE. Nevertheless, the circuit model accurately reproduces the phase dynamics of the coupled oscillator network from micromagnetic simulations and can be simulated in less than 1% of the time.

## V. STATISTICAL PERFORMANCE

Finally, we scale the HSPICE circuit model to larger coupled oscillator networks to study the performance of the SHNO Ising machine. The graph topology we use is an undirected ( $J_{ij} = J_{ji}$ ) Mobius ladder graph, as shown in Fig. 8(a) for the 16-node case. We focus on a common set of problems called MAX-CUT that involve partitioning a weighted graph into two subgraphs such that the sum of the edge weights  $w_{ij}$  linking nodes in the two subgraphs is maximized [13,66,67]. In the example shown in Fig. 8(a), this is to find a cut line (dotted curve) that maximizes  $\sum_{\text{cut}} w_{ij}$ , where the  $w_{ij}$  correspond to the edges connecting nodes from different subgraphs. MAX-CUT problems are mapped to the Ising Hamiltonian in Eq. (1) by coupling coefficients  $J_{ij} = -w_{ij}$  and spin values  $s_i$  representing the subgraph a node belongs to. When mapping between the edge weights  $w_{ij}$  and coupling conductances  $1/R_{ij}$ , we scale by a constant factor such that the coupling signal amplitude is bounded by  $V_{1f} \leq 88$  mV.

First, we demonstrate the scaling of the solution time and probability with the number of coupled oscillators  $n$ .

We use unweighted ( $w_{ij} = 1$ ) Mobius ladder graphs of sizes  $n = 16$ –256. Because the phase binarization process is slow for large arrays, an annealing schedule is employed where  $V_{2f}$  is stepped between 0 and 50 mV every 100 ns, resulting in strong phase binarization [5]. Graphs of this size are already difficult to solve by brute force calculation, but in this case the MAX-CUT solution always takes the form shown in Fig. 8(a) where the ground-state energy can be generalized as  $E_{GS}(n) = -\frac{3}{2}n + 4$  [67]. In Fig. 8(b), we show the probability of reaching the GS and a close-to-optimal solution (within 5% of the GS) as a function of  $n$ . Because of the simulation time overhead, thermal noise is not considered. The data are aggregated over 1000 simulations with randomly generated initial phase configurations. Though the GS probability falls to 17% by  $n = 256$ , the phases settle within 5% of the GS with over 85% probability even up to the largest simulated array. The inset to Fig. 8(b) shows a histogram of the final energy state distribution for  $n = 256$ . We see that the final phase states are consistently distributed among a few local energy minima very close to the GS, representing close-to-optimal solutions.

In Fig. 8(c), we show the time-to-solution  $t_{\text{sol}}$  to reach the GS with 99% certainty as a function of  $n$ , given by

$$t_{\text{sol}}(n) = t_{\text{run}}(n) \frac{\log(1 - 0.99)}{\log[1 - P_{\text{GS}}(n)]}, \quad (27)$$

where  $t_{\text{run}}$  is the runtime of each attempt at a given size and  $P_{\text{GS}}$  is the GS probability from Fig. 8(b) [6,8,61–63]. Compared to a 1 MHz LC oscillator Ising machine [6], the gigahertz SHNO Ising machine achieves solution times orders of magnitude lower due to the much higher operating frequency. The fast solution time

is arguably the most significant benefit of the SHNO Ising machine, as it enables solving larger and more difficult problems on reasonable timescales and with less energy.

Next, we study 16-node MAX-CUT problems on weighted Mobius ladder graphs with randomly generated coupling coefficients and thermal noise. We vary the bit resolution of the coupling coefficients  $J_{ij}$  from 0–6 bits, where higher-resolution problems are generally harder to solve due to having more complex energy landscapes with shallower energy minima [6]. Zero-bit resolution represents  $J_{ij} = \pm 1$ , while 6-bit coefficients take any nonzero integer value in  $[-2^6, 2^6]$ . A constant second harmonic signal with amplitude  $V_{2f} = 30$  mV is applied. For this relatively small scale problem, all the energy levels of the Ising Hamiltonian with all possible node states  $\{s_i\}$  can be enumerated using a brute force approach, providing a standard solution to compare to. In Fig. 9(a), we show the probability of reaching the GS or within three states of the GS ( $\leq \text{GS} + 3$ ) on an identical set of benchmark problems with and without thermal noise. Each set of results is aggregated over 1000 simulation runs with randomly generated coefficients and initial oscillator phases. Across all bit resolutions, thermal noise consistently increases the probability of reaching the ground state or another low-energy state, representing optimal and close-to-optimal solutions of the MAX-CUT problem. Histograms of the final energy states for 6-bit coefficients with and without thermal noise in Figs. 9(b) and 9(c) provide more insight into this trend. The presence of noise enables the oscillator phases to escape local energy minima and settle closer to the ground state, forming a higher concentration of low-energy states. The total number of nondegenerate phase states in this case is  $2^{15}$ , whereas the highest state observed in Figs. 9(b) and 9(c) is 58, indicating that the coupled oscillators reach very close-to-optimal solutions in all trials.

Finally, in Table II, we compare the solution time and energy consumption of the SHNO Ising machine against existing technologies. We solve MAX-CUT on unweighted randomly connected 100-node cubic graphs (where each node is connected to three others), as this is considered a more difficult architecture to solve than Mobius ladder graphs [10,67]. A similar annealing schedule is used as in Fig. 8, however with a duty cycle of 25% (150 ns off/50 ns on). We run ten simulations each of ten randomly generated graph instances with random initial phases, finding  $P_{\text{GS}} = 33\%$  across these 100 trials. As no closed-form expression exists for the ground-state energy, we use the BiqMac MAX-CUT solver to find the exact ground-state solution [68]. We neglect the power consumption of off-the-shelf amplifiers in our implementation. By using integrated on-chip amplifier circuits rather than off-the-shelf components to reduce the active power [69], we can potentially realize a significantly

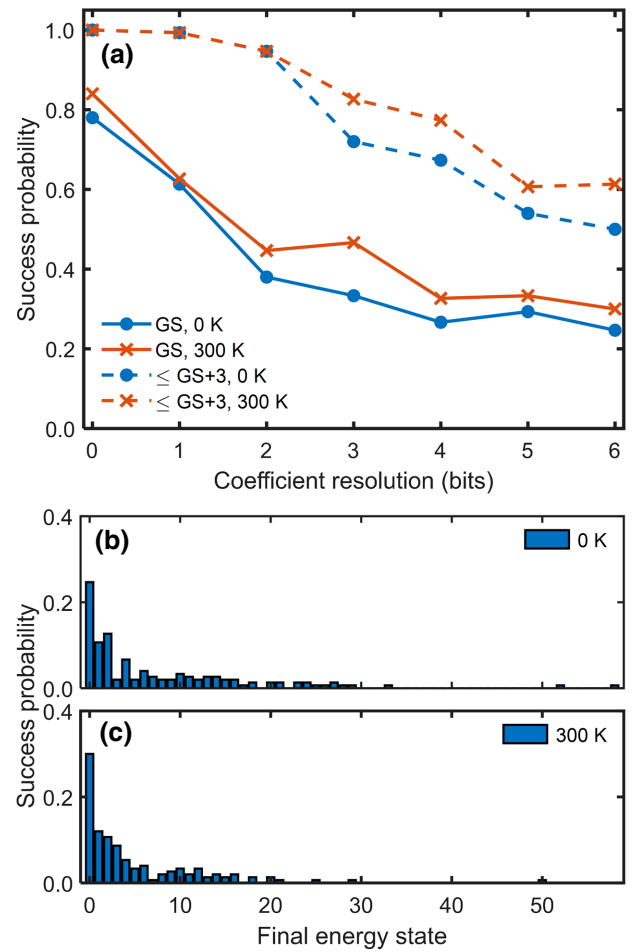


FIG. 9. (a) Probability of reaching the Ising Hamiltonian GS and within three states of the GS ( $\leq \text{GS} + 3$ ) versus coupling coefficient bit resolution with and without thermal noise. (b),(c) Histograms of final energy states for problems with 6-bit coefficients (b) without thermal noise and (c) with thermal noise. The ground state is 0, so lower-index states represent closer-to-optimal solutions.

more energy-efficient Ising machine than previous implementations.

While we focus on relatively sparse graphs for benchmarking purposes, the oscillator-based Ising machine architecture has potential to support all-to-all connectivity. Memristor crossbar arrays could be used to build such a system, as fully connected arrays larger than 1000 memristors have been demonstrated with reliable performance [6,70]. However, a number of nonideal effects may limit further scaling, including significant time delay in long interconnects (discussed briefly in Appendix D) and degradation of the resistance setting accuracy due to increasing parasitic wire resistances [71]. Alternatively, “virtual” all-to-all connectivity has been implemented in previous works by mapping fully connected problems to an equivalent Chimera graph with a greater number of vertices

TABLE II. Performance comparison between the SHNO Ising machine in this work and existing technologies. Time and energy values are standardized to size-100 MAX-CUT instances. Here D-WAVE denotes the D-WAVE 2000Q quantum annealing system, OPO denotes optical parametric oscillator, and PTNO denotes phase transition nano-oscillator.

	CPU [8]	GPU [61]	D-WAVE [62]	OPO [4,63]	LC [6,64]	PTNO [8,65]	SHNO [this work]
Graph architecture	Cubic	Cubic	Chimera	Cubic	Cubic	Cubic	Cubic
Coupling weights	Unweighted	Unweighted	$J_{ij} = \pm 1$	Unweighted	Unweighted	Unweighted	Unweighted
Solution time	246 ms	100 $\mu$ s	20 $\mu$ s <sup>a</sup>	150 ms	300 $\mu$ s	30 $\mu$ s	6.8 $\mu$ s
Power	60 W	< 250 W <sup>b</sup>	25 kW <sup>b</sup>		250 mW	2.56 mW	11.5 mW
Energy to solution	14.8 J	< 25 mJ	0.5 J		75 $\mu$ J	76.8 nJ	77.8 nJ
Energy efficiency (sol/s/W)	$6.7 \times 10^{-2}$	> 40	2		$1.3 \times 10^4$	$1.3 \times 10^7$	$1.3 \times 10^7$
Size (one element)				1 km fiber	0.1 mm <sup>2</sup>	0.2 $\mu$ m <sup>2</sup>	0.024 $\mu$ m <sup>2</sup>
Room temperature	Y	Y	N	Y	Y	Y	Y

<sup>a</sup>Solution time for problem instance of median difficulty.

<sup>b</sup>From publicly available hardware specifications on NVIDIA (GeForce GTX 1080 Ti) and D-WAVE (2000Q) websites, respectively.

[62,72] or implementing a time-, frequency-, or code-multiplexed scheme to increase the usage of the existing hardware resources [4,73]. Further technological development will be necessary to integrate the above approaches into our proposed SHNO-based coupling scheme, but these ideas represent interesting approaches toward modeling problems with general connectivity on the oscillator-based Ising machine.

## VI. CONCLUSION

In this paper, we present a detailed analytical study of the electrically coupled SHNO Ising machine. We begin by developing an ISF-based analytical model for the injection locking strength of a SHNO that can be used to model oscillators with nontrivial precession trajectories. By explicitly including the shape of the precession trajectory in our model, we can accurately predict injection locking not only at the oscillator's fundamental frequency but also at higher harmonic frequencies. We then integrate this model into a Verilog-A device for efficient circuit-level modeling of the Ising machine. Through scaling simulations, we demonstrate that the gigahertz-frequency SHNO array can solve combinatorial optimization problems on nanosecond timescales, achieving significant improvements in solution speed and energy efficiency compared to previously proposed Ising machines. Thermal phase noise is also expected to increase the probability of reaching the ground state or other low-energy states, allowing the SHNO Ising machine to be operated at room temperature. Our results provide useful quantitative insights and tools to enable the realization of a high-speed, energy-efficient, and ultra-scalable Ising machine employing SHNOs.

## ACKNOWLEDGMENTS

This work is supported by the MIT-IBM Watson AI lab. Micromagnetic simulations were performed on the

MIT/IBM Satori GPU supercomputers supported by the Massachusetts Green High Performance Computing Center (MGHPCC).

## APPENDIX A: MICROMAGNETIC SIMULATION OF THE SINGLE OSCILLATOR

For our micromagnetic simulations, we use the GPU-accelerated, open-source MUMAX<sup>3</sup> code [74]. The simulated SHNO has the general structure shown in Fig. 2(a). The in-plane dimensions of the MTJ are  $200 \times 120$  nm<sup>2</sup> ( $x \times y$ ) with a magnetic field  $B_{\text{ext}} = 20$  mT applied along the short axis of the MTJ. Only the Co-Fe-B free layer with thickness  $t_{\text{FL}} = 1.5$  nm is explicitly modeled with spin injection parameters assuming a Pt heavy metal layer with  $\theta_{\text{SH}} = 0.07$ . The Co-Fe-B material parameters are as follows: saturation magnetization  $M_s = 800$  kA/m, exchange stiffness  $A_{\text{ex}} = 13$  pJ/m, Gilbert damping  $\alpha = 0.02$ , perpendicular magnetic anisotropy constant  $K_u = 180$  kJ/m<sup>3</sup>. Because the injected spins are polarized in plane, a larger out-of-plane demagnetizing field (smaller PMA) should increase the oscillator phase sensitivity to spin torque based on Eq. (16), so we choose to reduce the out-of-plane demagnetizing field by only half. The free layer is discretized into cells with dimensions  $5 \times 5 \times 1.5$  nm<sup>3</sup> in  $x$ ,  $y$ , and  $z$ , respectively. The threshold dc voltage to observe auto-oscillations is  $V_c = 60$  mV [ $J_c = V_c / (R_{\text{HM}} w_{\text{HM}} t_{\text{HM}}) = 3.0 \times 10^{11}$  A/m<sup>2</sup>], and the dc operating point  $V_{\text{dc}} = 88$  mV ( $J_{\text{dc}} = 4.4 \times 10^{11}$  A/m<sup>2</sup>) is chosen for the large-angle oscillation in the  $x$ - $y$  plane. In micromagnetic simulations, the temperature is set to 0 K.

## APPENDIX B: MAGNETIC FIELD IMPULSE SENSITIVITY FUNCTION

The derivation of the ISF for magnetic field perturbation follows from a similar analysis as for the spin torque ISF

in Sec. III A. In this case, the general ISF expression is

$$\Gamma_{Bi}(t) = \frac{\Delta \tau_{Bi}}{B} \cdot \frac{\dot{\mathbf{m}}_{\text{eq}}}{|\dot{\mathbf{m}}_{\text{eq}}|^2}, \quad (\text{B1})$$

where  $i = \{x, y, z\}$  and  $B$  is the magnitude of the perturbing field. The relevant torque terms from Eq. (10) are the first and second terms; however, the second term is negligible due to low magnetic damping. The torque due to a perturbing magnetic field along the  $i$  direction (considered separate from the dc effective field  $\mathbf{B}_{\text{eff}}$ ) is then

$$\Delta \tau_{Bi} = -\gamma_e (\mathbf{m} \times \mathbf{B}_i). \quad (\text{B2})$$

The ISFs can again be represented by Fourier series as

$$\Gamma_{Bx}(t) = \frac{\omega_g \gamma_e}{2|\dot{\mathbf{m}}_{\text{eq}}|^2} \sum_{n=\text{odd}} b_n'' \frac{1}{n^2} \sin(n\psi), \quad (\text{B3})$$

$$\Gamma_{By}(t) = \frac{\omega_g \gamma_e}{|\dot{\mathbf{m}}_{\text{eq}}|^2} m_x m_z, \quad (\text{B4})$$

$$\Gamma_{Bz}(t) = \frac{\omega_g \gamma_e}{2|\dot{\mathbf{m}}_{\text{eq}}|^2} \sum_{n=\text{odd}} a_n'' \frac{1}{n^2} \cos(n\psi), \quad (\text{B5})$$

with nonzero coefficients

$$\begin{aligned} b_1'' &= (3m_y - 2m_{y0})m_z, \\ b_3'' &= m_y m_z, \\ a_1'' &= -(3m_y + 2m_{y0})m_x, \\ a_3'' &= m_x m_y. \end{aligned}$$

The ISFs in Eqs. (B3)–(B5) are plotted in Fig. 10. We see that the highest sensitivity to external field perturbations occurs at  $\psi = \pi/2$  and  $3\pi/2$ , where the conversion of thermal fluctuations [modeled as an effective field in

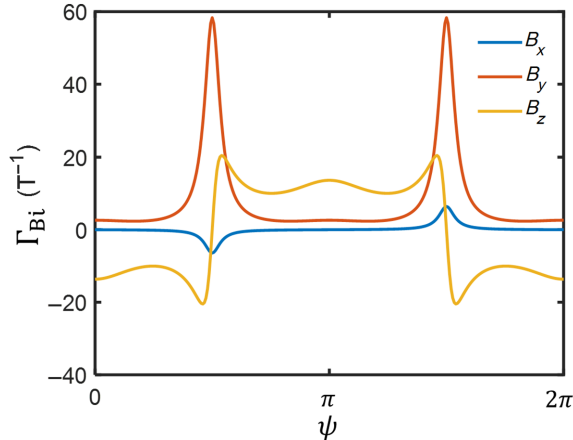


FIG. 10. ISFs for perturbation by magnetic fields along the  $x, y, z$  axes [Eqs. (B3)–(B5)] based on a SHNO with clamshell orbit.

Eq. (24)] to phase noise will be greatest. While it is not a focus of this paper, we note that one may use the ISF as a tool to analytically predict and design the phase noise performance of the oscillator [23,75].

### APPENDIX C: MICROMAGNETIC SIMULATION OF ELECTRICALLY COUPLED OSCILLATORS

The MUMAX<sup>3</sup> code is modified to enable simulation of electrical signal generation and coupling of up to four SHNOs [76]. The oscillators are simulated within a single strip geometry with dimensions  $6000 \times w_{\text{MTJ}} \times t_{\text{FL}} \text{ nm}^3$  and are each spaced apart by  $2 \mu\text{m}$  to minimize coupling via the stray fields. The devices used in the coupling simulations have the same parameters as the single device in Appendix A and the electrical parameters are the same as in HSPICE simulations (Table I).

To construct the electrical output signal of each oscillator, a magnetization-dependent quantity describing the oscillator magnetoresistance is defined in MUMAX<sup>3</sup>. The oscillating MTJ resistance assuming a fixed layer polarized along the  $+x$  axis is

$$R_{\text{out}}(t) = \frac{R_P - R_{\text{AP}}}{2} m_x(t) + \frac{R_P + R_{\text{AP}}}{2}. \quad (\text{C1})$$

Next, a MTJ read current density  $J_{\text{MTJ}}$  is specified. Gain elements are not modeled, so  $J_{\text{MTJ}}$  implicitly contains any necessary gain factor for the coupling signal. Finally, a six-element coupling conductance vector  $G_{ij} = [G_{11}, G_{12}, G_{13}, G_{23}, G_{24}, G_{34}]$  denoting the conductances linking oscillators  $i$  and  $j$  is specified to fully describe an all-to-all connected four-node network (Fig. 1).

A coupling current density is applied to SHNO  $i$  by adding the following expression to the existing spin transfer torque term in MUMAX<sup>3</sup>:

$$J_{\text{cpl},i} = J_{\text{MTJ}} \sum_{j,i \neq j}^4 G_{ij} \frac{R_P - R_{\text{AP}}}{2} m_{x,j}(t). \quad (\text{C2})$$

Modified versions of the RK45 and RK56 numerical solvers are written with Eq. (C2) appended to the MUMAX<sup>3</sup> equation set solved for each oscillator [74].

### APPENDIX D: TIME-DELAY COUPLING

When a finite time delay  $T_d$  exists in the coupling among a network of oscillators, Eq. (26) can be rewritten as

$$\begin{aligned} &V_{1f} \sin(\omega_g t + \phi_{e1}) \\ &= A_v \sum_{j=1}^N |V_{\text{out},j}| \frac{R_{\text{HM}}}{R_{ij}} \sin[\omega_g(t - T_d) + \phi_j]. \end{aligned} \quad (\text{D1})$$

The effects of such time delay can be analyzed using the oscillator's ISF [28]. When Eq. (D1) is integrated with the

ISF in Eq. (20), this time delay will produce a persistent phase shift  $[(\phi_i - \phi_j) \bmod \pi] = -\omega_g T_d$  in the resulting Adler's equation. Referring to Fig. 3(b), we see that this constant phase offset will produce a frequency shift (constant offset in  $d\phi/dt$ ) and asymmetry in the phase-locking bandwidth [28,57–59]. In a realistic circuit, to avoid such time-delay coupling complications, delay lines can be designed such that any phase shift around the coupling loop is fully compensated. Quantification of the SHNO Ising machine's robustness to coupling time delays will require further study. Our provided Verilog-A SHNO device model can be employed for theoretical studies along these lines, as the integrated ISF method accurately models the effects of time-delay coupling.

- 
- [1] D. Du and P. M. Pardalos, *Handbook of Combinatorial Optimization* Vol. 4 (Springer, Boston, MA, USA, 1998).
- [2] K. A. Smith, Neural networks for combinatorial optimization: A review of more than a decade of research, *INFORMS J. Comput.* **11**, 15 (1999).
- [3] E. Cohen and B. Tamir, Quantum annealing – foundations and frontiers, *Eur. Phys. J. Spec. Top.* **224**, 89 (2015).
- [4] T. Inagaki, Y. Haribara, K. Igarashi, T. Sonobe, S. Tamate, T. Honjo, A. Marandi, P. L. McMahon, T. Umeki, K. Enbutsu, O. Tadanaga, H. Takenouchi, K. Aihara, K.-i. Kawarabayashi, K. Inoue, S. Utsunomiya, and H. Takesue, A coherent Ising machine for 2000-node optimization problems, *Science* **354**, 603 (2016).
- [5] T. Wang and J. Roychowdhury, in *Unconventional Computation and Natural Computation*, edited by I. McQuillan and S. Seki (Springer International Publishing, Cham, Switzerland, 2019), p. 232.
- [6] J. Chou, S. Bramhavar, S. Ghosh, and W. Herzog, Analog coupled oscillator based weighted Ising machine, *Sci. Rep.* **9**, 14786 (2019).
- [7] S. Dutta, A. Khanna, and S. Datta, Understanding the continuous-time dynamics of phase-transition nano-oscillator-based Ising Hamiltonian solver, *IEEE J. Explor. Solid-State Comput.* **6**, 155 (2020).
- [8] S. Dutta, A. Khanna, A. S. Assoa, H. Paik, D. G. Schlom, Z. Toroczkai, A. Raychowdhury, and S. Datta, An Ising Hamiltonian solver based on coupled stochastic phase-transition nano-oscillators, *Nat. Electron.* **4**, 502 (2021).
- [9] A. Houshang, M. Zahedinejad, S. Muralidhar, J. Checinski, A. A. Awad, and J. Åkerman, A spin Hall Ising machine, arXiv preprint [ArXiv:2006.02236](https://arxiv.org/abs/2006.02236) (2020).
- [10] D. I. Albertsson, M. Zahedinejad, A. Houshang, R. Khymyn, J. Åkerman, and A. Rusu, Ultrafast Ising machines using spin torque nano-oscillators, *Appl. Phys. Lett.* **118**, 112404 (2021).
- [11] E. Kneller, J. Kranz, and W. Köster, *Beiträge zur Theorie des Ferromagnetismus und der Magnetisierungskurve* (Springer, Berlin, Heidelberg, Germany, 1956).
- [12] E. Ising, Beitrag zur theorie des ferromagnetismus, *Z. Phys.* **31**, 253 (1925).
- [13] R. M. Karp, On the computational complexity of combinatorial problems, *Networks* **5**, 45 (1975).
- [14] A. Lucas, Ising formulations of many NP problems, *Front. Phys.* **2**, 5 (2014).
- [15] R. Adler, A study of locking phenomena in oscillators, *Proc. IRE* **34**, 351 (1946).
- [16] Y. Kuramoto, Cooperative dynamics of oscillator community: A study based on lattice of rings, *Prog. Theor. Phys. Suppl.* **79**, 223 (1984).
- [17] S. Shinomoto and Y. O. Kuramoto, Phase transitions in active rotator systems, *Prog. Theor. Phys.* **75**, 1105 (1986).
- [18] S. I. Kiselev, J. C. Sankey, I. N. Krivorotov, N. C. Emley, R. J. Schoelkopf, R. A. Buhrman, and D. C. Ralph, Microwave oscillations of a nanomagnet driven by a spin-polarized current, *Nature* **425**, 380 (2003).
- [19] L. Liu, C.-F. Pai, D. C. Ralph, and R. A. Buhrman, Magnetic Oscillations Driven by the Spin Hall Effect in 3-Terminal Magnetic Tunnel Junction Devices, *Phys. Rev. Lett.* **109**, 186602 (2012).
- [20] A. N. Slavin and V. S. Tiberkevich, Nonlinear self-phase-locking effect in an array of current-driven magnetic nanocontacts, *Phys. Rev. B* **72**, 092407 (2005).
- [21] A. Slavin and V. Tiberkevich, Nonlinear auto-oscillator theory of microwave generation by spin-polarized current, *IEEE Trans. Magn.* **45**, 1875 (2009).
- [22] C. Serpico, R. Bonin, G. Bertotti, M. d'Aquino, and I. D. Mayergoyz, Theory of injection locking for large magnetization motion in spin-transfer nano-oscillators, *IEEE Trans. Magn.* **45**, 3441 (2009).
- [23] A. Hajimiri and T. Lee, A general theory of phase noise in electrical oscillators, *IEEE J. Solid-State Circuits* **33**, 179 (1998).
- [24] A. Demir, Floquet theory and non-linear perturbation analysis for oscillators with differential-algebraic equations, *Int. J. Circ. Theor. Appl.* **28**, 163 (2000).
- [25] F. Pepe, A. Bonfanti, S. Levantino, P. Maffezzoni, C. Samori, and A. L. Lacaita, in *2012 International Conference on Synthesis, Modeling, Analysis and Simulation Methods and Applications to Circuit Design (SMACD)* (2012), p. 17.
- [26] P. Maffezzoni, Synchronization analysis of two weakly coupled oscillators through a PPV macromodel, *IEEE Trans. Circuits Syst. I, Reg. Pap.* **57**, 654 (2010).
- [27] K. Kudo, T. Nagasawa, K. Mizushima, H. Suto, and R. Sato, Numerical simulation on temporal response of spin-torque oscillator to magnetic pulses, *Appl. Phys. Express* **3**, 043002 (2010).
- [28] V. S. Tiberkevich, R. S. Khymyn, H. X. Tang, and A. N. Slavin, Sensitivity to external signals and synchronization properties of a non-isochronous auto-oscillator with delayed feedback, *Sci. Rep.* **4**, 3873 (2014).
- [29] L. Landau and E. Lifshitz, in *Perspectives in Theoretical Physics*, edited by L. Pitaevski (Pergamon, Amsterdam, Netherlands, 1992), p. 51.
- [30] T. Gilbert, A phenomenological theory of damping in ferromagnetic materials, *IEEE Trans. Magn.* **40**, 3443 (2004).
- [31] J. Slonczewski, Current-driven excitation of magnetic multilayers, *J. Magn. Magn. Mater.* **159**, L1 (1996).
- [32] T. Brächer, P. Pirro, and B. Hillebrands, Parallel pumping for magnon spintronics: Amplification and manipulation of magnon spin currents on the micron-scale, *Phys. Rep.* **699**, 1 (2017).

- [33] A. G. Gurevich and G. A. Melkov, *Magnetization Oscillations and Waves* (CRC press, London, 2020).
- [34] A. V. Chumak, A. A. Serga, B. Hillebrands, G. A. Melkov, V. Tiberkevich, and A. N. Slavin, Parametrically stimulated recovery of a microwave signal using standing spin-wave modes of a magnetic film, *Phys. Rev. B* **79**, 014405 (2009).
- [35] G. A. Melkov, A. A. Serga, A. N. Slavin, V. S. Tiberkevich, A. N. Oleinik, and A. V. Bagada, Parametric interaction of magnetostatic waves with a nonstationary local pump, *J. Exp. Theor. Phys.* **89**, 1189 (1999).
- [36] S. Urazhdin, P. Tabor, V. Tiberkevich, and A. Slavin, Fractional Synchronization of Spin-Torque Nano-Oscillators, *Phys. Rev. Lett.* **105**, 104101 (2010).
- [37] B. Popescu, G. Csaba, D. Popescu, A. H. Fallahpour, P. Lugli, W. Porod, and M. Becherer, Simulation of coupled spin torque oscillators for pattern recognition, *J. Appl. Phys.* **124**, 152128 (2018).
- [38] B. Gu, K. Gullapalli, S. Hamm, B. Mulvaney, X. Lai, and J. Roychowdhury, in *Proc. 2005 IEEE International Behavioral Modeling and Simulation Workshop* (2005), p. 43.
- [39] X. Lai and J. Roychowdhury, Capturing oscillator injection locking via nonlinear phase-domain macromodels, *IEEE Trans. Microw. Theory Technol.* **52**, 2251 (2004).
- [40] X. Lai and J. Roychowdhury, in *IEEE MTT-S International Microwave Symposium Digest, 2005.* (2005), p. 871.
- [41] P. Maffezzoni and D. D'Amore, Phase-noise reduction in oscillators via small-signal injection, *IEEE Trans. Circuits Syst. I, Reg. Pap.* **58**, 2498 (2011).
- [42] T. Chen, A. Eklund, E. Iacocca, S. Rodriguez, B. G. Malm, J. Åkerman, and A. Rusu, Comprehensive and macrospin-based magnetic tunnel junction spin torque oscillator model-part II: Verilog-A model implementation, *IEEE Trans. Electron Devices* **62**, 1045 (2015).
- [43] S. Ahn, H. Lim, H. Shin, and S. Lee, Analytic model of spin-torque oscillators (STO) for circuit-level simulation, *JSTS: J. Semicond. Technol. Sci.* **13**, 28 (2013).
- [44] M. Kazemi, G. E. Rowlands, E. Ipek, R. A. Buhrman, and E. G. Friedman, Compact model for spin-orbit magnetic tunnel junctions, *IEEE Trans. Electron Devices* **63**, 848 (2016).
- [45] D. I. Albertsson, M. Zahedinejad, J. Åkerman, S. Rodriguez, and A. Rusu, Compact macrospin-based model of three-terminal spin-Hall nano oscillators, *IEEE Trans. Magn.* **55**, 1 (2019).
- [46] S. Mijalkovic, in *2006 25th International Conference on Microelectronics* (2006), p. 439.
- [47] G. Csaba, M. Pufall, W. Rippard, and W. Porod, in *2012 12th IEEE International Conference on Nanotechnology (IEEE-NANO)* (2012), p. 1.
- [48] G. D. Panagopoulos, C. Augustine, and K. Roy, Physics-based SPICE-compatible compact model for simulating hybrid MTJ/CMOS circuits, *IEEE Trans. Electron Devices* **60**, 2808 (2013).
- [49] S. Ament, N. Rangarajan, A. Parthasarathy, and S. Rakheja, Solving the stochastic Landau-Lifshitz-Gilbert-Slonczewski equation for monodomain nanomagnets: A survey and analysis of numerical techniques, *ArXiv:1607.04596* (2017).
- [50] K. Yogendra, C. Liyanagedera, D. Fan, Y. Shim, and K. Roy, Coupled spin-torque nano-oscillator-based computation: A simulation study, *J. Emerg. Technol. Comput. Syst.* **13**, 1 (2017).
- [51] Brooke McGoldrick, Verilog-A SHNO Macromodel. <https://github.com/bcmcgold/va-shno>.
- [52] W. F. Brown, Thermal fluctuations of a single-domain particle, *Phys. Rev.* **130**, 1677 (1963).
- [53] J. Xiao, A. Zangwill, and M. D. Stiles, Macrospin models of spin transfer dynamics, *Phys. Rev. B* **72**, 014446 (2005).
- [54] K. Yogendra, D. Fan, and K. Roy, Coupled spin torque nano oscillators for low power neural computation, *IEEE Trans. Magn.* **51**, 1 (2015).
- [55] K. Kudo and T. Morie, Self-feedback electrically coupled spin-Hall oscillator array for pattern-matching operation, *Appl. Phys. Express* **10**, 043001 (2017).
- [56] Y. V. Pershin and M. Di Ventra, Practical approach to programmable analog circuits with memristors, *IEEE Trans. Circuits and Syst. I: Reg. Pap.* **57**, 1857 (2010).
- [57] S. Tsunegi, E. Grimaldi, R. Lebrun, H. Kubota, A. S. Jenkins, K. Yakushiji, A. Fukushima, P. Bortolotti, J. Grollier, S. Yuasa, and V. Cros, Self-injection locking of a vortex spin torque oscillator by delayed feedback, *Sci. Rep.* **6**, 26849 (2016).
- [58] V. Tiberkevich, A. Slavin, E. Bankowski, and G. Gerhart, Phase-locking and frustration in an array of nonlinear spin-torque nano-oscillators, *Appl. Phys. Lett.* **95**, 262505 (2009).
- [59] G. Khalsa, M. D. Stiles, and J. Grollier, Critical current and linewidth reduction in spin-torque nano-oscillators by delayed self-injection, *Appl. Phys. Lett.* **106**, 242402 (2015).
- [60] <https://creativecommons.org/licenses/by/4.0/>.
- [61] A. D. King, W. Bernoudy, J. King, A. J. Berkley, and T. Lanting, Emulating the coherent Ising machine with a mean-field algorithm, *ArXiv:1806.08422* (2018).
- [62] S. Boixo, T. F. Rønnow, S. V. Isakov, Z. Wang, D. Wecker, D. A. Lidar, J. M. Martinis, and M. Troyer, Evidence for quantum annealing with more than one hundred qubits, *Nat. Phys.* **10**, 218 (2014).
- [63] P. L. McMahon, A. Marandi, Y. Haribara, R. Hamerly, C. Langrock, S. Tamate, T. Inagaki, H. Takesue, S. Utsunomiya, K. Aihara, R. L. Byer, M. M. Fejer, H. Mabuchi, and Y. Yamamoto, A fully programmable 100-spin coherent Ising machine with all-to-all connections, *Science* **354**, 614 (2016).
- [64] F. Chicco, A. Pezzotta, and C. C. Enz, in *2017 IEEE International Symposium on Circuits and Systems (ISCAS)* (IEEE, Baltimore, MD, USA, 2017), p. 1.
- [65] S. Dutta, A. Parihar, A. Khanna, J. Gomez, W. Chakraborty, M. Jerry, B. Grisafe, A. Raychowdhury, and S. Datta, Programmable coupled oscillators for synchronized locomotion, *Nat. Commun.* **10**, 3299 (2019).
- [66] M. Yannakakis, in *Proc. Tenth Annual ACM Symposium on Theory of Computing* (Association for Computing Machinery, New York, NY, USA, 1978), p. 253.
- [67] K. P. Kalinin and N. G. Berlof, Complexity continuum within Ising formulation of NP problems, *arXiv preprint ArXiv:2008.00466* (2020).
- [68] F. Rendl, G. Rinaldi, and A. Wiegele, Solving max-cut to optimality by intersecting semidefinite and polyhedral relaxations, *Math. Program.* **121**, 307 (2010).

- [69] T. Chen, Integration of GMR-based spin torque oscillators and CMOS circuitry, *Solid State Electron* **111**, 91 (2015).
- [70] C. Li, M. Hu, Y. Li, H. Jiang, N. Ge, E. Montgomery, J. Zhang, W. Song, N. Dávila, C. E. Graves, Z. Li, J. P. Strachan, P. Lin, Z. Wang, M. Barnell, Q. Wu, R. S. Williams, J. J. Yang, and Q. Xia, Analogue signal and image processing with large memristor crossbars, *Nat. Electron.* **1**, 52 (2018).
- [71] Y. Li, Z. Wang, R. Midya, Q. Xia, and J. J. Yang, Review of memristor devices in neuromorphic computing: Materials sciences and device challenges, *J. Phys. D: Appl. Phys.* **51**, 503002 (2018).
- [72] A. Rocchetto, S. C. Benjamin, and Y. Li, Stabilizers as a design tool for new forms of the Lechner-Hauke-Zoller annealer, *Sci. Adv.* **2**, e1601246 (2016).
- [73] N. Leroux, D. Marković, E. Martin, T. Petrisor, D. Querlioz, A. Mizrahi, and J. Grollier, Radio-Frequency Multiply-And-Accumulate Operations with Spintronic Synapses, *Phys. Rev. Appl.* **15**, 034067 (2021).
- [74] A. Vansteenkiste, J. Leliaert, M. Dvornik, M. Helsen, F. Garcia-Sanchez, and B. Van Waeyenberge, The design and verification of muMax3, *AIP Adv.* **4**, 107133 (2014).
- [75] A. Demir, A. Mehrotra, and J. Roychowdhury, Phase noise in oscillators: A unifying theory and numerical methods for characterization, *IEEE Trans. Circuits Syst. I. Fundam. Theory Appl.* **47**, 655 (2000).
- [76] Modified MUMAX<sup>3</sup> source code. <https://github.com/bcmcgold/3>.